2D MATERIALS

Correlated electron-hole state in twisted double-bilayer graphene

Peter Rickhaus[1]*, Folkert K. de Vries[1], Jihang Zhu[2], Elías Portoles[1], Giulia Zheng[1], Michele Masseroni[1], Annika Kurzmann[1], Takashi Taniguchi[3], Kenji Watanabe[3], Allan H. MacDonald[2], Thomas Ihn[1,4], Klaus Ensslin[1,4]

When twisted to angles near 1°, graphene multilayers provide a window on electron correlation physics. Here, we report the discovery of a correlated electron-hole state in double-bilayer graphene twisted to 2.37°. At this angle, the moiré states retain much of their isolated bilayer character, allowing their bilayer projections to be separately controlled by gates. We use this property to generate an energetic overlap between narrow isolated electron and hole bands with good nesting properties. Our measurements reveal the formation of ordered states with reconstructed Fermi surfaces, consistent with a density-wave state. This state can be tuned without introducing chemical dopants, enabling studies of correlated electron-hole states and their interplay with superconductivity.

Fermi surface nesting refers to electron and hole Fermi surfaces that map onto each other under translation by a nesting wave vector $\vec{Q}$. Because nesting implies a small band-energy cost for coherent superposition between electrons and holes, it favors interaction-driven broken-symmetry states. The nesting condition $\epsilon\left(\vec{k}_F + \vec{Q}\right) = -\epsilon\left(\vec{k}_F\right)$, where epsilon is a small energy offset from the Fermi energy and $\vec{k}_F$ is the Fermi wave vector, implies (*1*) that if two closed Fermi surfaces are perfectly nested, then they enclose the same area. Mixing two Fermi surfaces nested by wave vector $\vec{Q}$ leads to density-wave (DW) order with wavelength $2\pi/Q$. In the seminal theoretical work on DW states by Peierls (*2*), nesting occurs between like-spins in half-filled bands, the interactions are lattice mediated, and the DW is accompanied by a lattice distortion. DW states can also be favored by Coulomb interactions between electrons, in which case the lattice distortions (*3*) play only a parasitic role; the DW is then commonly referred to as an excitonic insulator (*4*). This term derives from viewing the order as a condensation of bosonic electron-hole pair states. Evidence for equilibrium excitonic condensation has been reported in 1T-$TiSe_2$ (*5*), in Sb nanoflakes (*3*), and in double quantum wells at high magnetic fields (*6*, *7*). Furthermore, notable progress toward quasi-equilibrium exciton condensation has been achieved in a $MoSe_2$/WSe_2 heterostructure under the application of a large interlayer bias (*8*). Condensation of nonequilibrium excitons and polaritons in optically pumped electron-hole fluids has also been studied extensively (*9*). Correlated electron-hole states continue to attract attention owing to their rich intrinsic physics and their close relationship to superconductivity (*10*).

Twisting van der Waals materials, including graphene bilayers (twisted bilayer graphene) (*11*–*16*) and double Bernal bilayers [twisted double-bilayer graphene (TDBG)] (*17*–*23*), is a proven strategy to engineer moiré bands that favor strongly correlated electronic states. In this study, we seek to realize electron-hole bands that are both nested and relatively narrow. To this end, we have studied the properties of TDBG (*17*–*23*) at intermediate twist angles, where the layer coupling is strong enough to form moiré bands but weak enough to retain the polarizability of decoupled bilayers (*24*–*27*). This polarizability can be quantified by the probability prob(κ_t) to find a band state at the κ_t-point (Brillouin zone corner of the top bilayer) in the top bilayer. If prob(κ_t) is large, which is the case at large twist angles, applying a displacement field D will charge the top bilayer with electrons and the bottom bilayer with holes (Fig. 1A). But correlated electron-hole states are fragile and, if they occur, only indirectly observable (*26*). Thus, the correlation strength needs to be maximized by approaching smaller angles where the narrowed moiré bands have a larger effective mass m^* (Fig. 1B). In figs. S18 and S19, we discuss the dependence of prob(κ_t) and m^*

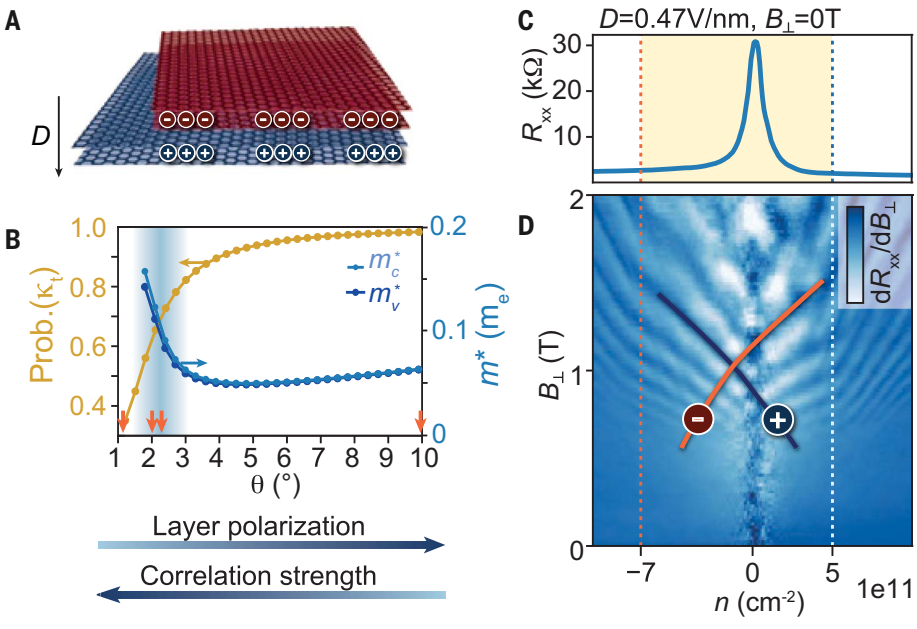

Fig. 1. Designed DW state in a moiré double bilayer. (**A**) Applying an electric field D to TDBG will charge the top and bottom bilayers with electrons and holes, respectively. (**B**) The layer polarization is given by prob(κ_t), and the correlation strength scales with the effective mass m^*. m_c^* (m_v^*) is the effective mass of the conduction (valence) band. Prob(κ_t)(θ) and $m^*(\theta)$ (at layer energy difference Δ_V = 30meV, see below) are obtained from band structure calculations at θ = 2.3°, showing that twists in the intermediate range (shaded region) combine strong polarizations and large masses and are favorable for DW formation. The red arrows mark twist angles at which measurements in fig. S4 are presented. (**C**) A peak in R_{xx} occurs at D = 0.47 V/nm and carrier density n = 0 in a TDBG device with θ = 2.37° and is consistent with a thermally activated gap (fig. S5). The yellow-shaded region represents the density range in which electron and hole bands coexist. (**D**) The bilayer's Landau fan diagram demonstrates that the gap appears inside a regime with both electron and hole bands, as confirmed by the presence of SdH resistance peaks (overlayed by orange and blue lines) that have opposite n versus $B_\perp$ slopes. Measurements are performed at temperature T = 1.2 K.

[1]Solid State Physics Laboratory, ETH Zürich, CH-8093 Zürich, Switzerland. [2]Department of Physics, University of Texas at Austin, Austin, TX 78712, USA. [3]National Institute for Material Science, 1-1 Namiki, Tsukuba 305-0044, Japan. [4]Quantum Center, ETH Zürich, 8093 Zürich, Switzerland.
*Corresponding author. Email: peterri@phys.ethz.ch

on twist angle and external field using the Bistritzer-MacDonald model (*28*), which is extended to the TDBG case.

In this study, we show that correlated electron-hole states are favored to form in the intermediate twist angle regime, roughly between 2° and 3°. Figure 1, C and D, summarizes the main experimental findings at θ = 2.37°. We observe a resistance peak at zero total density $n = 0$ and displacement field $D = 0.47$ V/nm (Fig. 1C), which appears when electrons and holes with approximately the same density coexist. This coexistence is evident in Landau fan measurements (Fig. 1D), which reveal electron and hole minibands that cross in energy.

A side-view schematic of our device is shown in Fig. 2A. We tune the density $n = (C_t V_t + C_b V_b)/e$ and displacement field $D = (C_b V_b - C_t V_t)/2\epsilon_0$ by applying voltages V_t and V_b to top and back gate electrodes. Here, C_t and C_b are the corresponding capacitances per unit area. The resistance peak in Fig. 1C is measured using the contact geometry in Fig. 2B. From the decrease of the resistance peak with increasing temperature (fig. S5), we extract a gap Δ using the Arrhenius law $R_{xx} \propto \exp(\Delta/2k_BT)$, where k_B is the Boltzmann constant. The extracted dependence of Δ on D at total density $n = 0$ is shown in Fig. 2C. The data reveal a gap around $D = 0$ (gray line) that closes with increasing $|D|$. Another gap is opened at large $|D|$ (yellow line).

To identify the conditions for the formation of the gap, we present measurements of Shubnikov–de Haas (SdH) oscillations for different n and D. In Fig. 2, D and E, we plot the numerical derivative of the inverse resistance $\partial/\partial n\ (1/R_{xx})$ (this quantity is chosen for best visibility of the relevant features) measured in a perpendicular magnetic field $B_\perp = 1.5$T. Along the dashed line at $D = 0$ in Fig. 2E, the spacing between SdH oscillations corresponds to a band degeneracy $g = 8$. The degeneracy is lifted by changing D, and SdH lines with two slopes emerge (indicated with arrows) in the dark blue and dark purple regions. In the light blue and light purple regions, the pattern changes, and lines with $g = 4$ that are parallel to the $n = 0$ line are seen. The slope of the SdH lines then changes again in the yellow region, and the oscillations become weaker.

These observations suggest the presence of two subbands in the dark regions. Their energy offset is tuned by D, and thus the subbands are related to the top and bottom bilayers (*27*, *29*). In the light blue and light purple regions, only one subband exists, and SdH oscillations are independent of D. Because the displacement field changes the energetic offset of the subbands, the phase at large D and small n (yellow region), which contains two subbands, corresponds to an electron-hole fluid, in agreement with the slopes in the Landau fan diagram Fig. 1D. Importantly, the observed gap at $n = 0$ and large D occurs in the midst of this two-subband region, thus strongly suggesting that it originates from charge carrier correlations. The region boundaries are well described using an electrostatic model based on parabolic subbands (figs. S8 and S9, where we also discuss the observed asymmetry with respect to n).

The experimental findings are in line with the single-particle band structures shown in Fig. 2, F to H, at θ = 2.3° for different adjacent layer on-site energy differences Δ_V [for conversion of D to Δ_V and the slight difference in θ = 2.37° between theory and experiment, see (*30*)]. At $\Delta_V = 0$ (Fig. 2F), two subbands of the fourfold spin and valley degenerate bilayer graphene emerge near the κ_t and κ_b points, leading to a degeneracy $g = 8$. Changing Δ_V (or D) breaks the layer degeneracy. For finite Δ_V, single-band regions with $g = 4$ emerge (Fig. 2, G and H). Around charge neutrality, bands with opposite carrier type coexist and the bandgap is closed. In contrast to the two gaps that we observe in Fig. 2C, only the gap at $n = 0$ (band energy $E = 0$) and $\Delta_V = 0$ is captured by the single-particle band structure (Fig. 2F). This gap originates from a combination of crystal fields, which leads to electron transfer from the outer to the inner layers (*31*) and localized states in the moiré lattice (*32*). The absence of a gap at $n = 0$ and finite Δ_V in the single-particle band structure agrees with our previous suggestion that the experimental gap in this region emerges from electron-hole correlations.

We now discuss the dependence of the correlated gap on the parameters D and n, which change the sizes of the electron-hole Fermi surfaces. We show the two-terminal conductance G as a function of dc source-drain bias voltage V_{sd} in Fig. 3A and observe coherence peaks at $n = 0$ and large D, suggesting the formation of a coherent ground state. In agreement with thermal activation measurements, the gap size Δ increases with D. At $D = 0.47$ V/nm

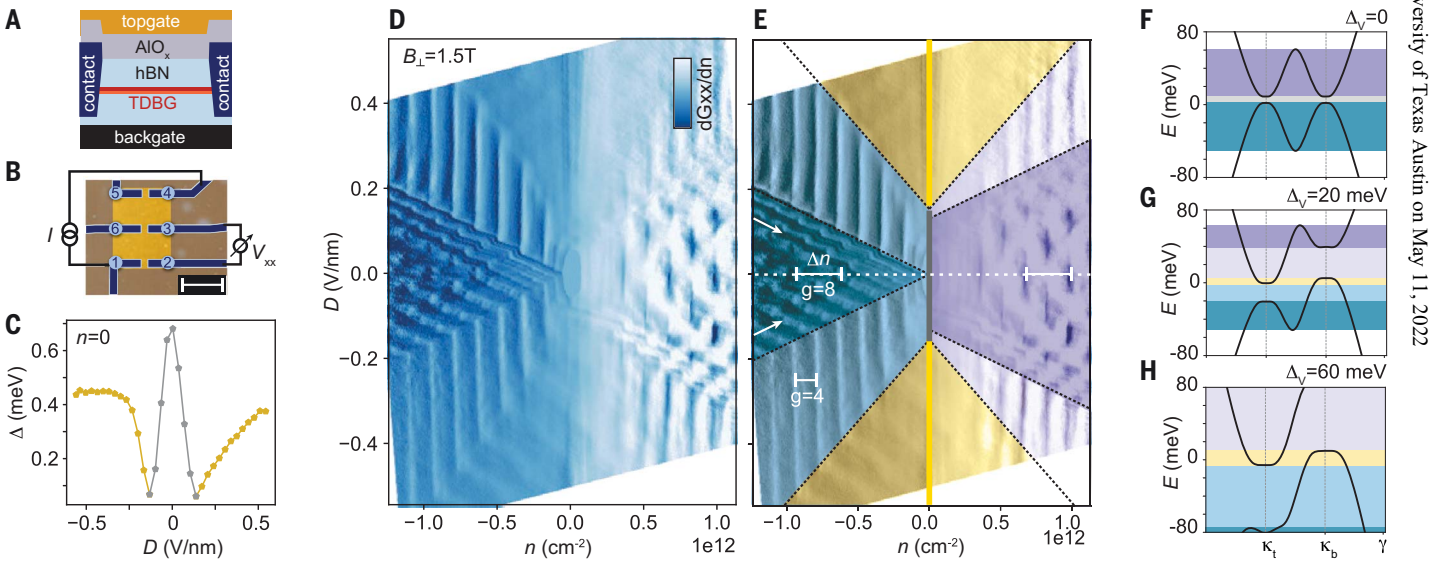

Fig. 2. Establishing electron-hole fluids. (**A** and **B**) Side view (A) and top view (B) of the stack. $R_{xx} \equiv V_{23}/I_{14}$, where V is the measured voltage drop and I is the applied current. Scale bar is 2 μm. hBN, hexagonal boron nitride. (**C**) From thermal activation measurements, we obtain Δ(D). Data highlighted with yellow color are taken in a regime where electron and hole bands coexist, whereas the gray colored data are taken for parameters where a single-particle gap is expected. (**D** and **E**) $\partial/\partial n\ (1/R_{xx})(D, n)$ at $B_\perp = 1.5$T and $T = 1.2$ K exhibits SdH oscillations that distinguish the regions highlighted in (E). In the yellow regions, electrons and holes coexist. The gray dashed lines mark the band edges at the κ_t and κ_b points. (**F** to **H**) Single-particle band structures for three values of $\Delta_V \propto D$.

and $n = 0$, $\Delta \approx 5$ meV (Δ is determined by the inflection points). We note that the thermal activation energy and the bias gap differ by an order of magnitude here. We speculate that this originates from complex thermal breakdown of the correlated gap and estimate that the bias measurement overestimates Δ by ~10% by additional series resistances (*30*). In Fig. 3B, we show the evolution of $\Delta(n)$ at $D = 0.47$ V/nm. Upon increasing n, the gap smears out and vanishes at $n \approx 2.5 \times 10^{11}$ cm^{-2}.

The correlated electron-hole gap vanishes with decreasing $|D|$ and increasing $|n|$. The first effect indicates the importance of effective mass and Fermi surface size, both of which increase with increasing $|D|$, as sketched in Fig. 3C. Conversely, the $|n|$ dependence suggests that an increasing asymmetry between electron and hole Fermi surfaces (blue and red) weakens the gap, as depicted in Fig. 3D. The observation that a correlated state emerges once Fermi surfaces match in size (at $n = 0$), and that the gap falters for small asymmetry, strongly suggests that the nesting of Fermi surfaces (i.e., contours in two dimensions) plays a crucial role for the formation of the correlated state.

We can probe this hypothesis by shifting the Fermi surfaces using a magnetic field. The concept of such a measurement in parallel field is depicted in Fig. 4A. At finite $B_\parallel$, the bands shift by the Zeeman energy. Now, nesting (equal Fermi surface) between opposite magnetic moments is possible at $n = 0$, whereas nesting between same magnetic moments is possible at $n \neq 0$. Indeed, the measured $R_{xx}(n, B_\parallel)$ traces are consistent with this concept (Fig. 4B). At $B_\parallel = 8$T, a shoulder in resistance at finite n is visible, consistent with a partially gapped band structure where half of the carriers form a correlated state while the other magnetic moment-bands remain conducting. The width of the shoulder (in n) increases with the Zeeman energy. How the region of enhanced resistance changes as a function of $|B_\parallel|$ and D can be observed in Fig. 4C. We can model the dependence on Zeeman energy by a basic model, yielding the dashed lines in Fig. 4C (for details, see fig. S10)

The behavior in perpendicular magnetic field $B_\perp$ is more complex. In Fig. 4D, we show $G(V_{sd}, D = 0.47\text{V/nm})$ traces for different $B_\perp$. We see that the gap is closed at a critical field $B_c = 4$T (orange trace) whose $B_c(D)$-dependence is plotted in the inset. In a semiclassical picture, the bands shift with $B_\perp$ owing to the valley-Zeeman effect. The valley g-factor in bilayer graphene $g_v \sim 20$ to 120 (*33*) has opposite signs in conduction and valence bands (see fig. S16 for details). $B_\perp$ therefore increases both electron and hole densities in one valley and decreases both in the other valley, as illustrated in Fig. 4E. If the correlated electron-hole gap is formed by wave function nesting, the gap in one valley (dashed bands–yellow gap) increases with $B_\perp$ and decreases in the other valley (solid bands–red gap). Thus, the completely gapped part of the band structure is decreasing with $B_\perp$, in agreement with the observations. In this picture, the gap opening for $B_\perp > B_c$ (green) can be interpreted as a single-particle gap at K' (green in Fig. 4E) and a correlated gap at K, i.e., as the formation of a valley-polarized correlated state.

The observations in magnetic field are consistent with basic models that assume Fermi surface nesting. We now confirm nesting of electron-hole surfaces by Hartree-Fock (HF) calculations where we incorporate the Coulomb potential and calculate the correlated gap Δ self-consistently (see fig. S13). Note that the moiré potential is not relevant for the emerging correlations because tunneling between top and bottom bilayers is weak at the intermediate twist in the relevant energy range. From HF calculations, we obtain the correlated bands, as shown in fig. S13, A and B. A gap is opened by electron-hole correlation and increases with adjacent layer on-site energy difference Δ_V. Both the gap size and the increase with displacement field agree with experiments, as shown in fig. S13C. We point out that this behavior is a result of decreasing static dielectric constant $\epsilon(\mathbf{q})$ with D (see fig. S20).

We note that Fermi surfaces in the same valley (e.g., κ_t and κ_b) are not perfectly circular even at $n = 0$, owing to interlayer tunneling between the middle two monolayers. However, the Fermi surfaces of opposite valleys (e.g., κ_t and κ'_b) match, suggesting that the correlated state is formed out of charge carriers from opposite valleys at $n = 0$. We show the calculated Fermi surfaces in fig. S14.

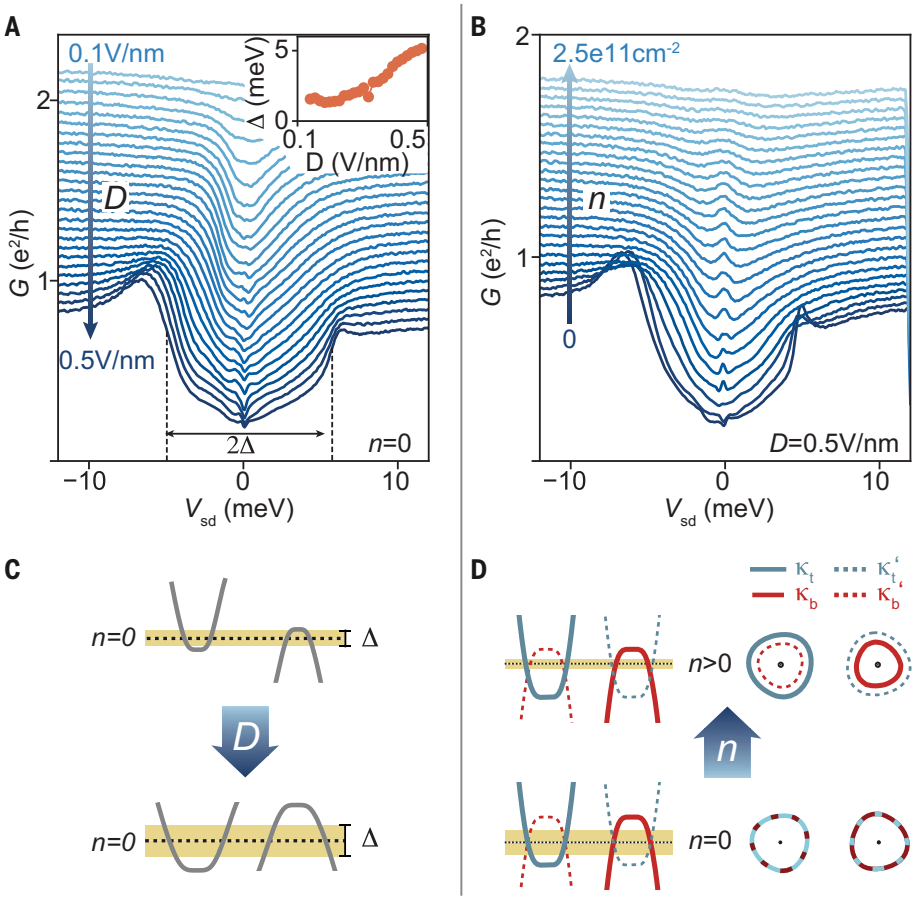

Fig. 3. Nesting. (**A**) Measurements of $G(V_{sd}, D)$ at $T = 0.1$ K reveal the appearance of a gap Δ. Curves are offset from the $D = 0.47$ V/nm trace. The inset shows extracted $\Delta(D)$, revealing that Δ increases with D. (**B**) $G(V_{sd}, n)$ at $D = 0.47$ V/nm showing that the gap vanishes with increasing n, where Fermi surface nesting falters. Curves are offset for clarity. (**C**) The top graphic shows a situation of finite D where electron and hole bands overlap and open a correlated gap Δ. By increasing D (bottom), Δ, the size of Fermi surfaces at $n = 0$, and masses m^* increase. (**D**) Calculated dispersion and Fermi surface around κ_t (blue) and κ_b (red) in the K (solid) and K' (dashed) valley, shown for a zero and finite n (for details, see fig. S14).

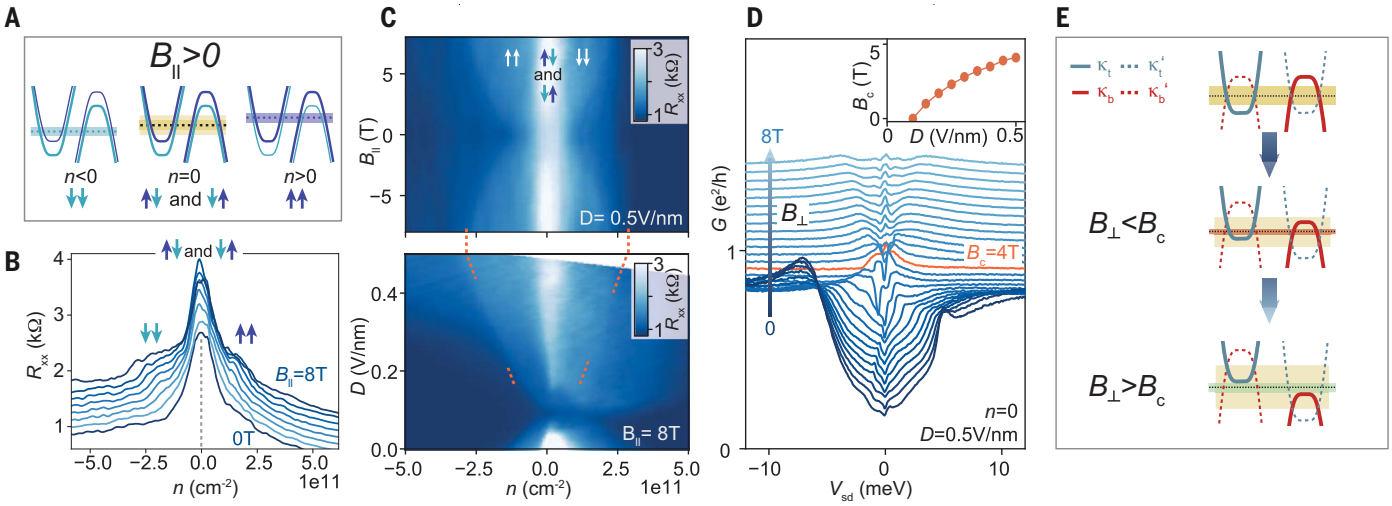

Fig. 4. Spin-polarized correlated gap. (**A**) Sketch of band structures under an applied $B_\parallel$ at different n. For a given $n < 0$ ($n > 0$), the turquoise (blue) bands with same magnetic moment have equal Fermi surface and thus open a gap, which is shaded turquoise (blue). At $n = 0$, bands with opposite magnetic moment (turquoise and blue) can form a gap (yellow-shaded region). The arrows indicate the magnetic moments of the charge carriers. (**B**) The partially gapped regions [turquoise-, yellow-, and blue-shaded regions in (A)] lead to an increase in R_{xx} with $B_\parallel$ at finite n. Curves are offset for clarity. (**C**) $R_{xx}(B_\parallel, n, D = 0.47\text{V/nm})$ and $R_{xx}(D, n, B_\parallel = 8\text{T})$ maps. The orange lines are calculated using $\Delta(D)$ and m^* from the experiment, without fitting parameters. (**D**) $G(V_{sd}, D = 0.5\text{V/nm})$ for increasing $B_\perp$. The gap is closed at $B_\perp = B_c$ (orange line). Curves are offset for clarity. In the inset, we plot the critical field, B_c, as a function of D. (**E**) The microscopic valleys K (solid) and K' (dashed) around κ_t (blue) and κ_b (red) shift in energy with $B_\perp$. For $B_\perp < B_c$, solid lines form a small gap (red-shaded region) and dashed lines a large gap (yellow-shaded region) corresponding to same-valley pairing at $n = 0$. For $B_\perp > B_c$, a single-particle gap (green-shaded region) is formed between the solid lines. For simplicity, Zeeman splitting is not sketched. All measurements in the figure are taken at $T = 0.1$ K.

Our model allows us to adjust the interlayer hopping parameter γ_1 between dimer sites in each bilayer to change m^*. The effective mass m^* generally depends on Δ_V, interlayer tunneling between the middle layers w, tunneling between the dimer sites within a Bernal bilayer γ_1, twist angle θ, and Fermi velocity v_F. If $w \neq 0$, changing w, θ, or Δ_V will change both m^* and layer polarization prob(κ_t). If $w = 0$, changing θ or Δ_V will have no effect on m^*, whereas changing γ_1 or v_F tunes m^* without any effect on layer polarizations. To investigate the effect of m^* solely on the correlated gap, we adjust the interlayer hopping parameter γ_1 (eq. S30) between the dimer sites in each bilayer. We observe an almost linear increase $\Delta(m^*)$ (see fig. S13D), supporting our previous statement that m^* determines the correlation strength (Fig. 1B). Theory does not show a strong dependence of pairing on the momentum difference between Fermi surfaces, only on the effective mass. This is in agreement with the excitonic character of a DW. In summary, the gap opening in HF calculations suggests that the correlated electron-hole state is consistent with a DW.

The correlated electron-hole state can be viewed as an excitonic insulator and is expected to exhibit counterflow superfluidity. Quantum phase transitions between DWs and disordered states can be controlled without chemical doping by varying n, or by varying D at $n = 0$, and such tunability could provide a new window on non–Fermi liquid physics.

REFERENCES AND NOTES

1. D. I. Khomskii, *Basic Aspects of The Quantum Theory of Solids* (Cambridge Univ. Press, 2010).
2. R. Peierls, *Ann. Phys.* **396**, 121–148 (1930).
3. Z. Li *et al.*, *Nano Lett.* **19**, 4960–4964 (2019).
4. D. Jérome, T. M. Rice, W. Kohn, *Phys. Rev.* **158**, 462–475 (1967).
5. A. Kogar *et al.*, *Science* **358**, 1314–1317 (2017).
6. I. B. Spielman, J. P. Eisenstein, L. N. Pfeiffer, K. W. West, *Phys. Rev. Lett.* **84**, 5808–5811 (2000).
7. L. Du *et al.*, *Nat. Commun.* **8**, 1971 (2017).
8. Z. Wang *et al.*, *Nature* **574**, 76–80 (2019).
9. H. Deng, H. Haug, Y. Yamamoto, *Rev. Mod. Phys.* **82**, 1489–1537 (2010).
10. J. Chang *et al.*, *Nat. Phys.* **8**, 871–876 (2012).
11. Y. Cao *et al.*, *Phys. Rev. Lett.* **117**, 116804 (2016).
12. Y. Cao *et al.*, *Nature* **556**, 43–50 (2018).
13. A. L. Sharpe *et al.*, *Science* **365**, 605–608 (2019).
14. M. Yankowitz *et al.*, *Science* **363**, 1059–1064 (2019).
15. P. Stepanov *et al.*, *Nature* **583**, 375–378 (2020).
16. Y. Saito, J. Ge, K. Watanabe, T. Taniguchi, A. F. Young, *Nat. Phys.* **16**, 926–930 (2020).
17. M. Koshino, *Phys. Rev. B* **99**, 235406 (2019).
18. N. R. Chebrolu, B. L. Chittari, J. Jung, *Phys. Rev. B* **99**, 235417 (2019).
19. Y. W. Choi, H. J. Choi, *Phys. Rev. B* **100**, 201402 (2019).
20. X. Liu *et al.*, *Nature* **583**, 221–225 (2020).
21. C. Shen *et al.*, *Nat. Phys.* **16**, 520–525 (2020).
22. G. W. Burg *et al.*, *Phys. Rev. Lett.* **123**, 197702 (2019).
23. M. He *et al.*, *Nat. Phys.* **17**, 26–30 (2021).
24. A. Luican *et al.*, *Phys. Rev. Lett.* **106**, 126802 (2011).
25. J. D. Sanchez-Yamagishi *et al.*, *Phys. Rev. Lett.* **108**, 076601 (2012).
26. G. W. Burg *et al.*, *Phys. Rev. Lett.* **120**, 177702 (2018).
27. F. K. de Vries *et al.*, *Phys. Rev. Lett.* **125**, 176801 (2020).
28. R. Bistritzer, A. H. MacDonald, *Proc. Natl. Acad. Sci. U.S.A.* **108**, 12233–12237 (2011).
29. P. Rickhaus *et al.*, *Sci. Adv.* **6**, eaay8409 (2020).
30. See materials and methods in the supplementary materials.
31. P. Rickhaus *et al.*, *Nano Lett.* **19**, 8821–8828 (2019).
32. F. J. Culchac, R. R. Del Grande, R. B. Capaz, L. Chico, E. S. Morell, *Nanoscale* **12**, 5014–5020 (2020).
33. Y. Lee *et al.*, *Phys. Rev. Lett.* **124**, 126802 (2020).
34. P. Rickhaus, Script repository: Electron-hole correlated state in twisted double bilayer graphene. ETH Library, ETH Zürich (2021); http://doi.org/10.5905/ethz-1007-405.

ACKNOWLEDGMENTS

Funding: We acknowledge financial support from the European Graphene Flagship and the Swiss National Science Foundation through NCCR Quantum Science and the ERC Syngery Grant Quantropy. P.R. acknowledges financial support from the ETH Fellowship program. Growth of hexagonal boron nitride crystals was supported by the Elemental Strategy Initiative conducted by Ministry of Education, Culture, Sports, Science and Technology (MEXT), Japan, and the Core Research for Evolutional Science and Technology (CREST) (JPMJCR15F3), Japan Science and Technology Agency (JST). A.H.M. and J.Z. were supported by the National Science Foundation (NSF) through the Center for Dynamics and Control of Materials, an NSF Materials Research Science and Engineering Center (MRSEC) under cooperative agreement no. DMR-1720595; and by the Welch Foundation under grant TBF1473. **Author contributions:** P.R. fabricated the devices; P.R., F.K.d.V., E.P., and G.Z. performed measurements; and P.R., F.K.d.V., E.P., G.Z., M.M., and A.K. were involved in data analysis. T.T. and K.W. provided hexagonal boron nitride crystals. P.R. wrote the manuscript, and P.R., F.K.d.V., E.P., G.Z., J.Z., A.H.M., T.I., and K.E. were involved in reviewing the manuscript. J.Z. performed simulations. A.H.M., T.I., and K.E. supervised the work. **Competing interests:** The authors have no competing interests. **Data and materials availability:** All data and code are available at ETH Library (*34*).

SUPPLEMENTARY MATERIALS

https://science.org/doi/10.1126/science.abc3534
Materials and Methods
Supplementary Text
Figs. S1 to S20
References (*35*–*41*)

24 April 2020; accepted 11 August 2021
10.1126/science.abc3534

Science

Correlated electron-hole state in twisted double-bilayer graphene

Peter RickhausFolkert K. de VriesJihang ZhuElías PortolesGiulia ZhengMichele MasseroniAnnika KurzmannTakashi TaniguchiKenji WatanabeAllan H. MacDonaldThomas IhnKlaus Ensslin

Science, 373 (6560), • DOI: 10.1126/science.abc3534

Fermi nesting

Correlated states have been shown to emerge in bilayer and trilayer graphene with the two-dimensional layers at just the right angle with respect to each other. Key to the enhanced importance of interactions are the so-called moiré electronic bands that form in such systems. Rickhaus *et al*. explored a related system of two graphene bilayers twisted with respect to each other. The twist angle was set so that the layer coupling was strong enough to form moiré bands but weak enough for the carrier concentration in the top and bottom bilayer to be controlled separately. Doping the top bilayer with electrons and the bottom bilayer with holes, the researchers created a correlated state with nested Fermi surfaces. —JS

Science (ISSN) is published by the American Association for the Advancement of Science. 1200 New York Avenue NW, Washington, DC 20005. The title *Science* is a registered trademark of AAAS.